Absolute Activity Quantitation in Simultaneous $^{123}I/^{99m}Tc$ Brain SPECT

Georges El Fakhri, Stephen C. Moore, Philippe Maksud, André Aurengo, and Marie Foley Kijewski

Department of Radiology, Harvard Medical School and Brigham and Women's Hospital, Boston, Massachusetts; and U494 INSERM, CHU Pitié-Salpêtrière, Paris, France

Dual-isotope imaging can allow simultaneous assessment of brain perfusion using a ^{99m}Tc-labeled tracer and neurotransmission using an ^{123}I-labeled tracer. However, the images are affected by scatter, cross talk, attenuation, distance-dependent collimator response (DCR), and partial-volume effect. We determined the accuracy and precision of activity quantitation in simulated normal and pathologic studies of simultaneous $^{123}I/^{99m}Tc$ brain SPECT when compensating for all degrading phenomena. **Methods:** Monte Carlo simulations were performed using the Zubal brain phantom. Contamination caused by high-energy ^{123}I decay photons was incorporated. Twenty-four ^{99m}Tc and ^{123}I activity distributions were simulated on the basis of normal and pathologic patient activity distributions. Cross talk and scatter were corrected using a new method based on a multilayer perceptron artificial neural network (ANN), as well as by the asymmetric window (AW) approach; for comparison, unscattered (U) photons of ^{99m}Tc and ^{123}I were recorded. Nonuniform attenuation and DCR were modeled in an iterative ordered-subset expectation maximization (OSEM) algorithm. Mean percentage biases and SDs over the 12 normal and 12 pathologic simulated studies were computed for each structure with respect to the known activity distributions. **Results:** For ^{123}I, AW + OSEM yielded a bias of 7% in the cerebellum, 21% in the frontal cortex, and 36% in the corpus callosum in the simulated normal population. The bias was increased significantly in the striata of simulated pathologic studies ($P < 0.05$). The bias associated with ANN was significantly lower (<9% in these brain structures, $P < 0.05$). For ^{99m}Tc with AW + OSEM, the bias was 60% in the corpus callosum, 36% in the striata, and 18%–22% in the cortical lobes in the simulated normal population. This bias was <11% in all brain structures with ANN. In the simulated pathologic population, the bias associated with AW increased significantly in the cortical lobes to 55% ($P < 0.05$), although it did not change significantly with ANN. **Conclusion:** The accuracy and variability over simulated normal and pathologic studies of both ^{99m}Tc and ^{123}I activity estimates were very close with ANN to those obtained with U + OSEM. ANN + OSEM is a promising approach for absolute activity quantitation in simultaneous $^{99m}Tc/^{123}I$ SPECT.

Key Words: dual-isotope brain SPECT; absolute quantitation; Monte Carlo simulation; artificial neural network; cross-talk compensation

J Nucl Med 2001; 42:300–308

Received Apr. 3, 2000; revision accepted Aug. 14, 2000.

For correspondence or reprints contact: Georges El Fakhri, PhD, Department of Radiology, Brigham and Women's Hospital, Boston, MA 02115.

Dual-isotope imaging ($^{123}I/^{99m}Tc$) has potential clinical applications in the simultaneous assessment of neurotransmission and brain perfusion. ^{123}I tracers allow imaging of both presynaptic (e.g., 2β-carbomethoxy-3β-(4-iodophenyl)tropane (*1*)) and postsynaptic (e.g., iodobenzamide [IBZM] (*2*)) phases of dopaminergic transmission and have potential clinical use in various movement disorders including Parkinson's disease, Huntington's disease, progressive supranuclear palsy, multiple-system atrophy, and Wilson's disease (*3*), whereas ^{99m}Tc tracers (e.g., hexamethylpropyleneamine oxime [HMPAO] or ethylcysteinate dimer) allow the assessment of brain perfusion. Furthermore, simultaneous acquisition of ^{123}I and ^{99m}Tc studies reduces the acquisition time while allowing perfect registration of perfusion and neurotransmission studies. Despite these advantages, this technique has not been routinely implemented in the clinic. Because the emission energies of ^{99m}Tc (140 keV) and ^{123}I (159 keV) are close, not only are scattered ^{123}I photons detected in the ^{99m}Tc window, but, equally important, primary photons of each radionuclide are detected in the wrong window (cross talk) (*4*). Furthermore, like all SPECT images, dual-isotope images are affected by attenuation and both distance-dependent and intrinsic components of collimator and detector response. Previous physical phantom studies of dual-isotope $^{99m}Tc/^{123}I$ imaging, with cross-talk correction by simple energy windowing techniques, yielded conflicting results: Ivanovic et al. (*5*) reported major limitations, whereas Devous et al. (*6,7*) obtained accurate quantitation.

Artificial neural networks (ANNs) were used previously to correct for scatter in ^{99m}Tc SPECT studies (*8,9*). In previous work, we proposed two original approaches to correct for cross talk and scatter based on constrained factor analysis and ANNs (*10*); we found the latter more promising. The aim of this study was to assess the quantitation accuracy and precision that could be achieved in normal and pathologic dual brain studies when correcting for scatter and cross talk using ANN, for attenuation and variable collimator response using an iterative ordered-subset expectation maximization (OSEM) algorithm, and for the residual partial-volume effect (PVE) using three-dimensional recovery coefficients. Results were compared with those of a spectral

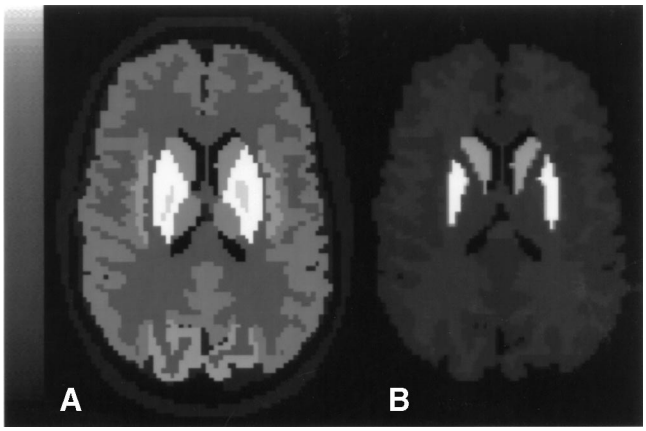

FIGURE 1. Reference simulated ^{99m}Tc (A) and ^{123}I (B) activity distributions in representative slice of normal patient.

asymmetric window (AW) approach (*6*) and with the primary or unscattered (U) photon distributions in Monte Carlo simulations of 24 dual-isotope ^{99m}Tc/^{123}I studies of a digitized human brain. In all cases, the accuracy and precision of activity estimates were determined with respect to the true activity distributions simulated in each brain structure.

MATERIALS AND METHODS

Monte Carlo Simulations of Dual ^{123}I/^{99m}Tc Studies

Human Brain Phantom. A digitized human brain phantom (*11*) was used to model normal and pathologic activity distributions of ^{99m}Tc and ^{123}I. Activity distributions in 60 brain structures, including the cerebellum, caudate nucleus, putamen, corpus callosum, hippocampus, and cortical lobes (frontal, prefrontal, temporal, parietal, and occipital), were modeled on the basis of activities reported in normal patients with ^{99m}Tc-HMPAO (*12*) and ^{123}I-IBZM (*13*) or in nonhuman primates with ^{123}I-Altropane ([^{123}I]IACFT,2β-carbomethoxy-3β-(4-fluoraphenyl)-n-(1-iodoprop-1-en-3-yl)nortropane) (*14*). ^{99m}Tc and ^{123}I reference activity distributions are shown in Figure 1 in a representative slice of one of the simulated normal patients. Monte Carlo simulations were used to generate 24 dual-isotope studies that included 12 normal brain scans and 12 scans of patients with a reduced uptake of either or both tracers.

The normal population consisted of four noise realizations of each of three normal distributions of ^{99m}Tc and ^{123}I. The ^{99m}Tc/^{123}I activity ratios in many brain structures are listed in Table 1. The ratios in all structures of normal 2 were half those of normal 1, whereas those of normal 3 were twice those of normal 1. The pathologic population consisted of three groups, each comprising four patients. Patients in the first group had normal cortical perfusion distributions and reduced striatal ^{123}I activity (25% or 50% ^{123}I uptake reduction in the caudate nucleus and putamen, and normal ^{123}I uptake in other brain structures) to mimic patients with Parkinson's disease (e.g., patient 4 in Table 1). The second group consisted of four patients with normal ^{123}I neurotransmission distributions but with a 50% reduction of ^{99m}Tc uptake in either temporal and frontal or temporal and parietal lobes to mimic Alzheimer's disease (e.g., patient 5 in Table 1). The third group consisted of four patients with pathologic perfusion and neurotransmission scans (e.g., patient 6 in Table 1), as in diffuse Lewy body dementia (*15*).

Monte Carlo Simulations. We enhanced the SimSet Monte Carlo code (*16*) to incorporate coherent scatter in the phantom. A lookup table of attenuation coefficients, at 1-keV increments over the range 50–600 keV, was established for each structure; structures were assumed to be homogeneous within their boundaries. The ^{99m}Tc and ^{123}I distributions were simulated separately, with 986 million decays for each ^{99m}Tc distribution and 768 million decays for each ^{123}I distribution. Variance reduction techniques, namely, stratification and forced detection (*17*), yielded approximately 350 million and 240 million detected photons, respectively, for each ^{99m}Tc and ^{123}I simulated distribution. Scattered photons were followed for up to nine scattering events. When tracking photons through an E.CAM low-energy, high-resolution (LEHR) collimator (Siemens, Knoxville, TN), only the geometric component of the collimator response was modeled, assuming a 15-cm radius of rotation. For each study, 128 projections, each 128 $\times$ 64 pixels, were generated over 360°. The intrinsic energy resolution was modeled by a gaussian distribution with an energy-dependent full width at half maximum (FWHM). The Monte Carlo events were sorted by energy, position, and nature (primary or scattered); twenty-six 4-keV-wide energy windows ranging from 79 to 183 keV were used. The voxel size was 2.4 mm in the *x*, *y*, and *z* directions.

Modeling ^{123}I High-Energy Contamination. Low-abundance (<3.5%), high-energy ^{123}I photons emitted at 346, 440, 505, and 529 keV were simulated using a more comprehensive technique for a spheric phantom (2-cm-diameter spheric source of ^{123}I centered within a 15.7-cm-diameter sphere). The Monte Carlo code, previously developed by our group, modeled all details of the photon transport

TABLE 1
^{99m}Tc to ^{123}I Activity Ratios in Several Simulated Brain Structures for Six Simulated Dual-Isotope Studies

Study	Cerebellum (10,550)	Corpus callosum (764)	Frontal cortex (8,671)	Parietal cortex (9,368)	Occipital cortex (5,407)	Caudate nucleus (776)	Putamen (738)
1. Normal 1	3.85	2.53	3.47	3.65	3.82	0.96	1.07
2. Normal 2	1.93	1.27	1.74	1.83	1.91	0.48	0.54
3. Normal 3	7.70	5.06	6.94	7.30	7.64	1.92	2.14
4. Reduced ^{123}I	3.85	2.53	3.47	3.65	3.82	1.92	2.14
5. Reduced ^{99m}Tc	3.85	2.53	1.74	1.77	3.82	0.92	1.07
6. Reduced ^{123}I and ^{99m}Tc	3.85	2.53	1.74	1.77	3.82	0.92	2.14

Numbers in parentheses are number of voxels.

through the collimator and detector, including Compton and coherent scatter and penetration through the collimator septa, as well as backscatter from camera components behind the NaI(Tl) crystal (*18*). The same LEHR collimator was simulated.

The energy and spatial distributions of the high-energy contamination were determined by comparing spectra and projection datasets arising solely from the 159-keV decay photons to those of the high-energy contaminant decay photons. We ascertained that throughout the energy range of interest (85–189 keV), no high-frequency information was visible. In fact, the contaminant projection images in each energy window were very well fitted to slowly decreasing, linear functions of the distance from the center of the "brain" sphere, extending all the way to the edge of the camera's field of view. On the other hand, the projection images from the appropriately collimated 159-keV photons clearly showed a sharp boundary between the small, high-concentration sphere and the surrounding low-concentration sphere. These observations gave us confidence that the high-energy contamination could be well described by a simple parametric model, and that differences between contamination generated by the spheric phantom and that from the realistic brain phantom would be minor. We adopted the following hybrid algorithm for estimating and adding the high-energy contribution to projection datasets simulated for the anatomically correct brain phantom:

- Compute the total ^{123}I counts obtained in each projection dataset (from the brain phantom simulation) within the energy range of 150.5–174.5 keV.
- For each 4-keV-wide energy window in the interval of 84.5–188.5 keV, multiply the total counts from the first step by an appropriate scale factor derived from the two-sphere simulation results to estimate the total number of high-energy contaminant counts expected in the projection image at this energy.
- Parameterize the spatial distribution of the contaminant counts in each energy window using a linearly decreasing function of distance from the center of the brain in the projection: contamination(x,y) = a − (b × r), where r = sqrt(x^2 + y^2). The shape parameters a and b, obtained by fitting results of the two-sphere simulation, were, in turn, parameterized as slowly varying polynomial functions of energy. Each resulting image was then scaled to yield the total number of contaminant counts expected from the second step and added to the brain projection image simulated solely from the 159-keV decay photons.

Finally, Poisson noise at levels corresponding to 1 min of acquisition time per projection was added to both the ^{99m}Tc projections and ^{123}I projections in each energy window.

Cross-Talk and Scatter Correction

We compensated for cross talk and scatter using the AW and ANN approaches. For the AW method (*6*), windowed projections were generated using a 15% wide symmetric window for ^{99m}Tc and a 10% asymmetric window for ^{123}I starting at the center of the photopeak. We compensated for high-energy ^{123}I scatter by subtracting a uniform image of intensity equal to the mean measured number of counts in the background from the estimated brain projections. The projections corresponding to primary ^{99m}Tc and ^{123}I activity distributions (assuming perfect cross-talk and scatter corrections) were also generated.

ANN Architecture. The ANN devised for cross-talk and scatter correction is a multilayer perceptron (MP) using a back-propagation algorithm as a learning tool (*19*). It is made of partly connected artificial neurons organized in multiple layers. Each neuron has several inputs and one output. Inputs can be either external data or outputs of other neurons. The effect of each input is regulated through a specific weight established during the learning phase. A weighted sum of the inputs is used to calculate the internal state of the neuron. This activation value is then propagated to the following neurons. The MP was composed of an input layer (26 neurons), a hidden layer (13 neurons), and an output layer comprising 2 neurons (Fig. 2). For each pixel of each projection, the 26 neural network inputs were the energy values expressed as fractions of the total counts detected in all 26 energy channels. The two output neurons provided the ratio of estimated primary to total photons for ^{99m}Tc and ^{123}I in the pixel. All pixels in all projections were then processed sequentially by the neural network.

ANN Learning Phase. The ANN was trained using low-noise simulated projections of a phantom consisting of an elliptic cylinder of water surrounded by a thin layer of bone, with several spheres, cylinders, and parallelepipeds embedded inside. The technetium-to-iodine activity ratios of these structures ranged from 100:0 to 0:100 (*20*). Several representative technetium and iodine spectra, along with the true expected values of the primary-to-total photon ratio of each radionuclide, were submitted to the network. High-energy contamination was incorporated into the Monte Carlo simulation of the learning phantom as described above for the brain studies.

The learning set was divided into two groups: a training set was used for adjustment of the weights, and a validation set was used for testing global convergence. In our study, the number of examples in the training set exceeded by more than 40 times the number of weights, thereby excluding any overfitting problems. All 50,000 pixels in the projections of the learning phantom were used for training, except for 1,280 pixels (20 pixels × 64 projections) in a region of interest at the center of each projection that were used for validation. Data were presented to the network in 3,000 cycles to minimize both root-mean-squared error and likelihood criteria.

ANN Sensitivity Analysis. A sensitivity analysis (*21*) was performed to assess the importance of each of the 26 spectral window inputs in yielding accurate estimates of the true ^{99m}Tc and ^{123}I activity distributions. The estimation errors of ^{99m}Tc and ^{123}I distributions in the learning phantom were calculated while clamping one of the 26 inputs. Each input was individually clamped by replacing all pixels in the corresponding energy window by the mean pixel value over all projections in the dataset to determine an intermediate constant value of the clamped input. The importance of a specific input was gauged by measuring the effect of clamping that input on the output error. This analysis yielded 26 series, of 64 projections each, of ^{99m}Tc and ^{123}I activity estimates, each corresponding to the clamping of one input (C_{ep}, e = 1. . .26, p = 1. . .64). Next, the mean percentage error (MPE) over each projection p, for a given energy window input e, was calculated over the N_{ep} nonzero pixels of the projection C_{ep} with respect to the true estimate of ^{99m}Tc or ^{123}I activity distributions obtained when no energy channel was clamped (T_{ep}) (*1*).

$$MPE_{ep} = \frac{100}{N_{ep}} \sum_{i=1}^{N_{ep}} \frac{|C_{ep}(i) - T_{ep}(i)|}{T_{ep}(i)}. \qquad \text{Eq. 1}$$

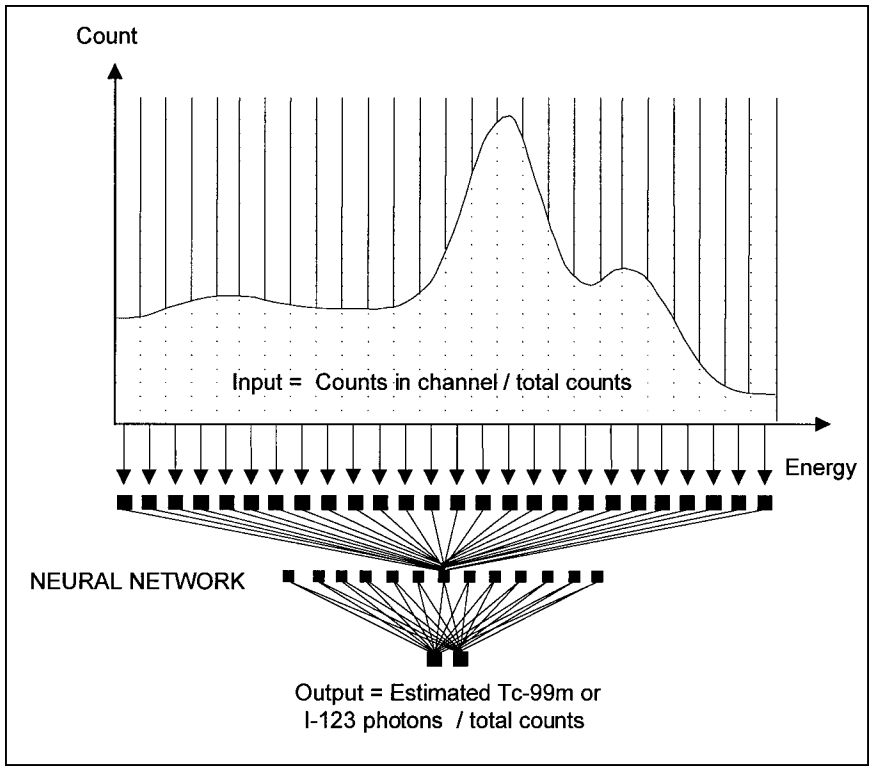

FIGURE 2. Architecture of ANN designed for cross-talk and scatter correction.

Attenuation and Distance-Dependent Collimator Response Corrections

Projections of ^{99m}Tc and ^{123}I, corrected for cross talk and scatter, were reconstructed using the maximum likelihood expectation maximization (EM) algorithm and an accelerated maximization algorithm based on the use of ordered subsets (OSEM) (*22*). The 128 projections of each radionuclide distribution were grouped into four subsets of projections. Fifteen iterations were performed; to reduce processing time, standard EM was applied during each subiteration using a subset of projections, as opposed to using the complete set of projections. Nonuniform attenuation was corrected directly in the reconstruction algorithm by modeling nonuniform attenuation in the projector/backprojector. The attenuation distributions used in the reconstruction algorithm were the reference simulated attenuation maps of brain tissues at 140 keV for ^{99m}Tc and at 159 keV for ^{123}I.

We compensated for the distance-dependent collimator response (DCR) by modeling the distance-dependent resolution in the projector/backprojector of the OSEM algorithm. The dependence of the FWHM on distance (d), calculated for the simulated LEHR collimator (FWHM [cm] = 0.139 + 0.048 d), was in good agreement with the relation measured on an actual E.CAM gamma camera (Siemens) equipped with the same collimator. Regularization was achieved using the kernel-sieve approach (*23*) by which gaussian filtering (σ = 0.14 cm) was applied to the final reconstructed image to reduce noise.

After 15 OSEM iterations, spatial resolution was uniform in the reconstructed images and approximately equal to the intrinsic resolution of the gamma camera (~0.35 cm). The residual spatial resolution significantly affects the measurement of activity concentrations in small structures, that is, the PVE. This effect is most pronounced for hot structures surrounded by cold background (*24*,*25*). This situation describes ^{123}I activity estimation in the caudate nucleus and putamen because ^{123}I uptake in the striata is five to seven times that of the surrounding brain tissue. To compensate for the PVE, the reference striatal volume containing a uniform number of counts per pixel (100) was convolved with a three-dimensional gaussian kernel of FWHM equal to that of the spatial resolution of the SPECT images after DCR correction. The ratio of the striatal counts in each voxel of the original image to that in the same voxel after convolution, namely, the voxel's recovery coefficient, was used to correct the striatal regions for the PVE, as proposed in other studies (*26*,*27*).

Data Analysis

Technetium and iodine activity concentrations within the structures of interest were calculated from reconstructed AW, ANN, and primary images. These concentrations were compared with the reference simulated activity distributions in each structure to assess quantitation accuracy and precision with the two cross-talk and scatter correction methods, as well as those with a hypothetic perfect cross-talk and scatter correction (primary photons). Accuracy and precision were assessed separately in the normal and pathologic groups of simulated patients. Mean ^{99m}Tc and ^{123}I uptakes were computed in the cerebellum, corpus callosum, hippocampus, frontal lobe, parietal lobe, temporal lobe, occipital lobe, caudate nucleus, and putamen for each of the 24 simulated studies, and percentage biases with respect to the corresponding reference activity distributions were calculated:

$$\text{percentage bias} = 100\left(\frac{\text{mean activity in corrected structure}}{\text{mean activity in primary structure}} - 1\right). \quad \text{Eq. 2}$$

A nonparametric Mann–Whitney test (*28*) was performed to assess the significance of observed differences between the mean

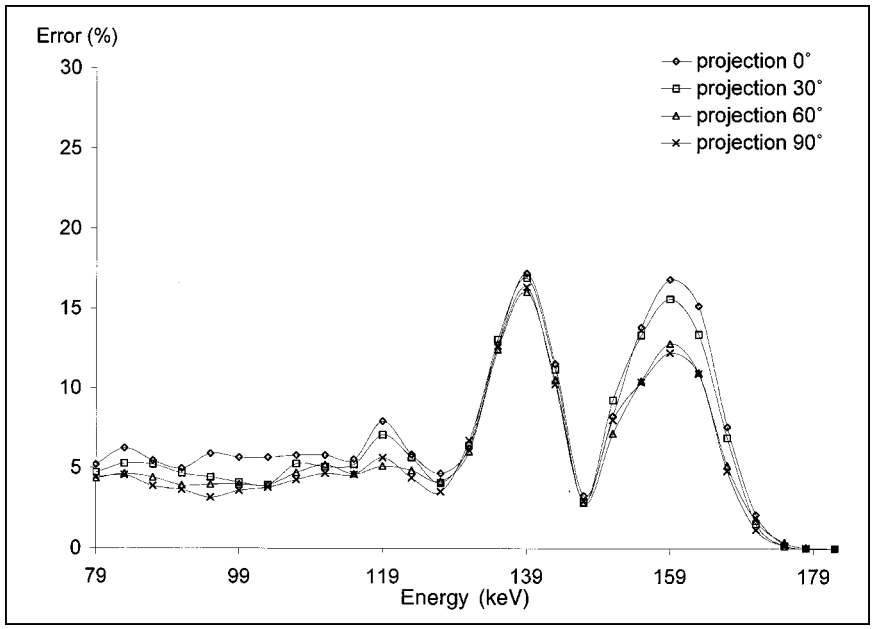

FIGURE 3. ^{99m}Tc sensitivity analysis: absolute mean percentage error with respect to true estimated ^{99m}Tc activity distribution in four different views when clamping the 26 energy channels one at a time.

uptakes in brain structures measured with AW and ANN, as well as with primary photons alone, in the normal or pathologic populations. Next, mean percentage bias and SD over the 12 normal or pathologic patients were computed for each structure with respect to the corresponding reference activity distributions.

RESULTS

Sensitivity Analysis of ANN

The absolute mean percentage errors in the estimated ^{99m}Tc and ^{123}I activity distributions are shown for four projections in Figures 3 and 4, respectively, after the clamping of individual energy channels. The energy channels were 4-keV wide and ranged from 79 to 183 keV. For ^{99m}Tc activity estimation, clamping one among the first 10 energy inputs (i.e., deleting spatial information in the corresponding energy channel) led to an error in the ANN output that varied between 4% and 6%, depending on the view (Fig. 3). This error did not vary greatly, however, with the energy of the clamped channel. On the other hand, clamping an energy input within either of the ^{99m}Tc or ^{123}I photo peaks resulted in substantial errors in estimating the ^{99m}Tc activity distribution. This error was close to 17% for all four views at 140 keV and varied from 11% to 17% at 159 keV. Finally, clamping the two inputs corresponding to 179 and 183 keV had no effect on the network output.

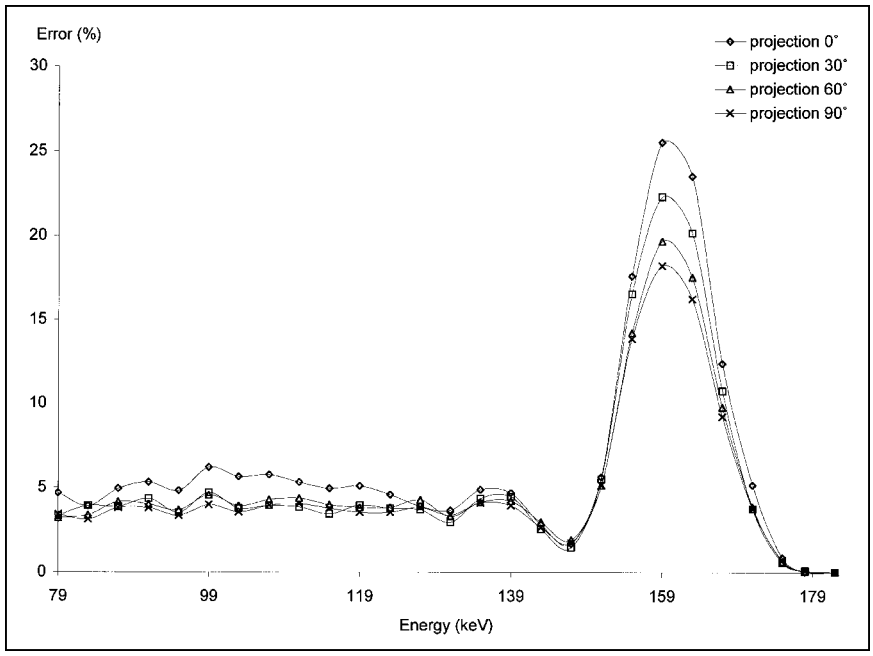

FIGURE 4. ^{123}I sensitivity analysis: absolute mean percentage error with respect to true estimated ^{123}I activity distribution in four different views when clamping the 26 energy channels one at a time.

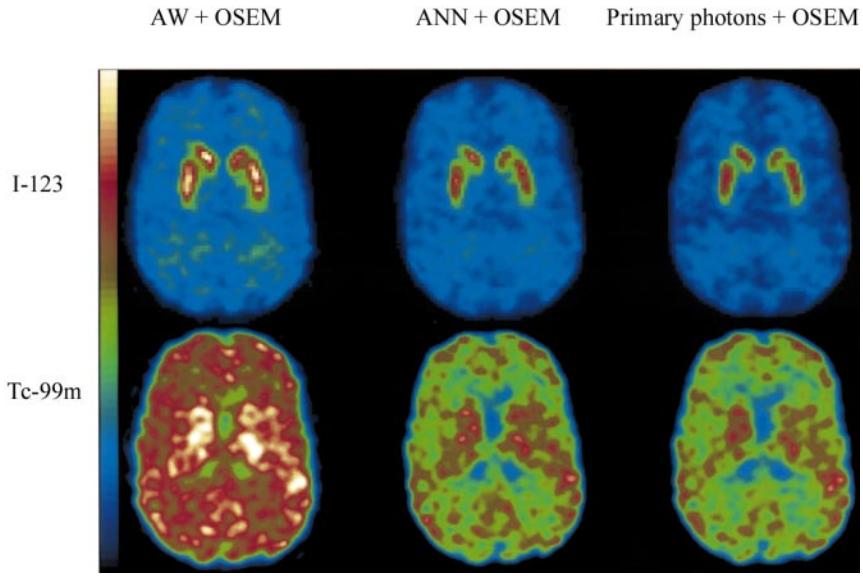

FIGURE 5. OSEM reconstructed ^{123}I and ^{99m}Tc distributions of AW, ANN, and primary photon distributions in normal patient with low ^{99m}Tc uptake for slice shown in Figure 1. Artifactually increased activity is seen in different brain structures in AW + OSEM ^{99m}Tc image.

For ^{123}I activity estimation, clamping any of the energy inputs between 79 and 135 keV yielded an error close to 5% in all views (Fig. 4). Clamping the energy inputs corresponding to the ^{123}I photopeak increased the output error to more than 18%. However, clamping energy inputs corresponding to the ^{99m}Tc photopeak had little effect on the estimation of ^{123}I activity.

Absolute Activity Quantitation of ^{123}I and ^{99m}Tc

^{99m}Tc and ^{123}I activity distributions with AW + OSEM, ANN + OSEM, and primary photons + OSEM are shown in Figure 5 for simulated patient normal 2 (Table 1). ^{99m}Tc and ^{123}I images are displayed as windowed to the same maximum for each radionuclide. The effects of ^{123}I contamination in the ^{99m}Tc image, as well as activity overestimation caused by cross talk, can be seen in the artifactually increased activity of the striata in the AW + OSEM ^{99m}Tc image and the artifactual uptake in the AW + OSEM ^{123}I image.

^{123}I Activity Quantitation. The mean bias and SD, calculated for each structure over the 12 normal or 12 pathologic patients with respect to the corresponding reference ^{123}I activity distributions, are shown in Table 2. ^{123}I activity quantitation bias varied considerably among structures of interest for AW + OSEM, and it was significantly greater than the bias associated with ANN + OSEM ($P < 0.05$) and the primary photon distribution U + OSEM ($P < 0.05$). Furthermore, the SD of this bias over the normal population was systematically greater with AW than with ANN and U in all brain structures under consideration. In comparing structures with similar ^{123}I reference uptake such as the cortical lobes, this bias was 21% in the temporal cortex and 30% in the parietal cortex with AW. The bias was <9% in all cortical lobes with ANN and was not significantly different between ANN and U. Likewise, the bias varied between 7% in the cerebellum and 36% in the corpus callosum with AW + OSEM, whereas it was <10% in both

TABLE 2
^{123}I Percentage Bias in 12 Normal and 12 Pathologic Simulated Studies for Several Brain Structures After Scatter, Cross-Talk, DCR, and Attenuation Corrections

Simulated study	Cerebellum	Corpus callosum	Frontal cortex	Parietal cortex	Occipital cortex	Caudate nucleus	Putamen	Caudate nucleus RC*	Putamen RC*
Normal									
AW + OSEM	7.4 ± 4.4	36.2 ± 2.7	21.1 ± 3.9	29.6 ± 4.2	24.0 ± 4.1	−16.8 ± 1.7	−18.9 ± 1.7	5.64 ± 1.8	3.6 ± 1.9
ANN + OSEM	−4.5 ± 1.6	9.1 ± 2.4	3.9 ± 2.7	8.6 ± 3.6	8.4 ± 3.2	−24.5 ± 0.7	−23.3 ± 0.6	−5.94 ± 0.9	−3.4 ± 1.0
Primary + OSEM	−3.8 ± 1.0	9.0 ± 1.1	5.6 ± 1.3	9.0 ± 1.5	4.8 ± 1.8	−21.0 ± 0.4	−26.1 ± 0.4	−1.64 ± 0.6	−2.9 ± 0.6
Pathologic									
AW + OSEM	11.3 ± 1.5	40.8 ± 1.7	21.7 ± 2.2	31.2 ± 2.4	24.5 ± 1.7	−13.0 ± 2.4	−9.1 ± 2.1	8.9 ± 3.6	12.4 ± 3.4
ANN + OSEM	−5.9 ± 0.9	10.7 ± 0.8	7.6 ± 1.6	8.0 ± 1.6	9.2 ± 1.3	−23.1 ± 1.2	−17.8 ± 1.1	−2.7 ± 1.6	2.3 ± 1.4
Primary + OSEM	−4.4 ± 0.6	8.8 ± 0.5	8.5 ± 0.7	7.7 ± 0.6	3.5 ± 0.9	−22.7 ± 0.6	−18.6 ± 0.6	−1.7 ± 0.9	1.5 ± 0.8

* Biases measured in striatal structures are shown without and with compensation for PVE using recovery coefficients (RC).

TABLE 3
^{99m}Tc Percentage Bias in 12 Normal and 12 Pathologic Simulated Studies for Several Brain Structures After Scatter, Cross-Talk, DCR, and Attenuation Corrections

Simulated study	Cerebellum	Corpus callosum	Frontal cortex	Parietal cortex	Occipital cortex	Caudate nucleus	Putamen
Normal							
AW + OSEM	20.3 ± 5.2	59.9 ± 8.8	21.6 ± 4.0	18.1 ± 4.5	21.3 ± 3.9	39.5 ± 10.3	35.6 ± 8.3
ANN + OSEM	1.4 ± 2.2	−6.2 ± 1.5	−6.5 ± 1.2	−9.7 ± 1.3	−11.4 ± 1.6	−4.3 ± 1.8	−5.0 ± 2.8
Primary + OSEM	−1.0 ± 0.8	3.1 ± 0.7	−2.9 ± 0.6	−5.5 ± 0.8	−7.3 ± 0.9	0.8 ± 0.9	−3.5 ± 0.8
Pathologic							
AW + OSEM	24.7 ± 5.5	54.4 ± 9.5	53.1 ± 8.0	55.7 ± 7.4	18.2 ± 4.2	38.2 ± 11.2	34.5 ± 9.0
ANN + OSEM	1.7 ± 0.9	−5.1 ± 0.8	5.9 ± 1.6	8.6 ± 1.6	−10.1 ± 1.4	−2.1 ± 1.2	−5.3 ± 1.1
Primary + OSEM	−1.0 ± 1.0	−3.8 ± 1.1	2.2 ± 0.7	7.1 ± 0.5	−8.4 ± 0.6	−2.4 ± 0.6	−3.8 ± 0.3

structures ($P < 0.05$) with ANN and with U. In the absence of PVE compensation, ^{123}I activity concentration in the striata was underestimated in all three volumes (bias was −19% with AW, −23% with ANN, and −26% with U in the putamen). When PVE was corrected using three-dimensional recovery coefficients, the bias became <5% with AW, ANN, and U + OSEM.

Patients showing pathologic patterns of dopaminergic transmission are characterized by a reduced uptake in the caudate nucleus and putamen. ^{123}I activity quantitation bias in such patients was not significantly different from that in normal patients with either AW or ANN + OSEM in the cortex, cerebellum, corpus callosum, and hippocampus ($P < 0.05$). However, a significant increase ($P < 0.05$) in bias was found with AW in the putamen (4% in normal and 12% in pathologic, after PVE correction). This result was not found with ANN, where bias in all structures was <10%. Furthermore, after PVE compensation, bias with ANN was not significantly different from that with U in the striata, frontal cortex, and parietal cortex (not significant [NS], $P < 0.05$).

^{99m}Tc Activity Quantitation. The mean bias and SD, calculated with respect to corresponding reference ^{99m}Tc distributions in normal and pathologic simulated populations, are shown in Table 3. In the normal population with AW + OSEM, cross talk led to a significant overestimation of the reference ^{99m}Tc activity distributions in all brain structures ($P < 0.05$); the mean percentage bias was 59% in the corpus callosum, 38% in the striata, and 20% in the cortical regions. The bias was significantly less with ANN + OSEM and U + OSEM (<2% in the cerebellum, 5% in the striata, and <11% in all brain structures, $P < 0.05$). Furthermore, ANN and U yielded systematically smaller SD, that is, better precision, than did AW.

A major limitation of AW was observed when assessing ^{99m}Tc activity quantitation in the pathologic population characterized by a reduced perfusion uptake in either the temporal and frontal lobes or temporal and parietal lobes. The bias was 54% in the frontal, parietal, and temporal lobes compared with 20% in the same lobes in the normal population ($P < 0.05$). The bias in the occipital lobe, where no perfusion defects were modeled, was similar to that reported for normal patients (18% compared with 21% previously). Likewise, the variance of the estimation of ^{99m}Tc activity in the three lobes was significantly greater than that seen in normal patients ($P < 0.05$). For ANN + OSEM, bias in pathologic patients was <10% in all four lobes and was not significantly different from that observed in normal patients (NS). This result also occurred with U + OSEM in the parietal and occipital cortex (NS, $P < 0.05$). The SD over the activity estimates was not significantly different with ANN in the pathologic population compared with that in the normal population. Finally, ^{99m}Tc estimation bias was 38% in the caudate nucleus with AW + OSEM compared with <3% with ANN and U + OSEM ($P < 0.05$).

DISCUSSION

Sensitivity Analysis of ANN

A sensitivity analysis was performed to assess the importance of the 26 energy inputs used in this study. The importance of each input was gauged by the output error of the network when the input was clamped in the learning phantom (*21*). Our results showed that this error was small (<5% [Figs. 3 and 4]) but not negligible for both ^{123}I and ^{99m}Tc when clamping any of the first 10 energy channels (79 keV < energy < 119 keV). This finding reveals that the network is robust to the absence of spatial information in any of the energy inputs in this energy range. However, the error did not decrease when clamping energy inputs <100 keV, suggesting that all low-energy inputs yielded useful information to the network. This result can be explained by the fact that the number of detected counts in low-energy windows (corresponding to high-order scattered photons) was far from negligible and depended strongly on projection angle and patient pathology. These errors observed when clamping low-energy inputs suggest that for a commercial instrument with few acquisition energy channels available, a wider energy input (e.g., 8-keV width) can be used for low

energies. Such an approach should be preferred to one that excludes low-energy channels. Furthermore, we did not model in this work the emission of characteristic lead (Pb) x-rays in the collimator. Spectral information from inputs below 100 keV can become even more important in the presence of x-ray emission because the shape of the spectrum will be significantly modified below 100 keV, and further investigation is required to assess the ability of the neural network to estimate accurately ^{99m}Tc and ^{123}I activity distributions in this case. Furthermore, clamping any energy input in the photopeak region of ^{99m}Tc or ^{123}I led to substantial errors in the ^{99m}Tc estimation. This finding reveals that both photopeak inputs were used in the estimation of the lower-energy radionuclide (^{99m}Tc) activity distribution. This situation did not occur for activity estimation of the higher-energy radionuclide (^{123}I), for which the errors did not increase significantly when the ^{99m}Tc photopeak inputs were clamped.

^{123}I and ^{99m}Tc Activity Quantitation

When assessing absolute activity quantitation, our results in both normal and pathologic patients showed that the primary reconstructed photon distributions (U + OSEM) were reasonably close to the reference ^{123}I and ^{99m}Tc activity distributions (bias $<$ 9% in all brain structures). Therefore, modeling nonuniform attenuation and DCR in the projector/backprojector of an iterative reconstruction algorithm such as OSEM is an effective approach to compensate for attenuation and DCR in brain SPECT. Furthermore, images obtained with ANN + OSEM were reasonably close to the reference activity distributions for both ^{123}I and ^{99m}Tc (bias $<$ 11% in all brain structures). This result showed that ANN + OSEM can yield more accurate and robust quantitation in dual ^{123}I/^{99m}Tc brain studies in healthy humans and pathologic patients compared with any previously reported technique. Biases were significantly higher with AW than with ANN; furthermore, they varied considerably among brain structures and increased significantly in pathologic, compared to normal, patients.

This study showed that absolute quantitation with accuracy ~10% can be achieved with ANN + OSEM in the challenging case of dual ^{99m}Tc and ^{123}I studies with cross-talk correction of both scattered and primary photons. Other dual-isotope or emission/transmission studies (e.g., ^{99m}Tc/^{153}Gd, ^{201}Tl/^{99m}Tc, ^{201}Tl/^{57}Co) with emission photopeaks farther apart than ^{99m}Tc and ^{123}I could potentially benefit from our approach to achieve more accurate quantitative imaging. The ANN + OSEM approach should also be applicable to the simpler case of scatter + attenuation + collimator response compensation in single-isotope brain SPECT.

For the striatal structures, we used a PVE correction method based on three-dimensional recovery coefficients measured for the structures of interest. For Monte Carlo simulations of digitized human brain phantoms, the reference image was used to define the correct boundary of the brain structure of interest. In patients, the reference image can be an anatomic image registered to the SPECT image such as a CT (*27*) or MRI scan. However, an important issue to be addressed in this latter case is the accuracy of patient registration between the functional and anatomic modalities. Compensation of PVE, combined with ANN + OSEM, reduced significantly ^{123}I activity bias in the striata from 25% to 6%. Our results for the caudate nucleus (776 voxels ~ 11 mL) are consistent with the 25% underestimation of activity reported by Gilland et al. (*29*) caused by PVE in a 12-mL sphere, with a comparable sphere-to-background ratio of ^{123}I.

Our approach assumes that background activity concentration is very small compared with that of the structure of interest. This assumption is true in the caudate nucleus and putamen in ^{123}I brain studies because the striatal activity concentration is five to seven times that of the surrounding tissue. Furthermore, when a structure's activity concentration is close to that of the surrounding background, the PVE is negligible because the counts lost by the finite resolution blurring are compensated by the counts added from surrounding regions caused by the same blurring. This situation occurred for the hippocampus and corpus callosum; both structures had sizes comparable with that of the putamen but contained simulated ^{123}I and ^{99m}Tc activity concentrations close to those of the surrounding tissues. As a result, no PVE was observed when estimating activity concentration in these regions. Our PVE compensation model is not applicable, however, for small structures with a relatively small uptake difference with respect to the surrounding tissue, and further investigation is required to compensate for PVE in this case.

Absolute activity quantitation was considered in this study. When considering relative quantitation (i.e., ratio of activity in the cortex to that in the cerebellum), the bias introduced by AW can become even more important because of the large error associated with the cerebellar activity estimates. For example, in regions with comparable ^{99m}Tc perfusion, such as the parietal cortex and the cerebellum (reference activity ratio = 0.92), the measured ratio of cortex to cerebellum was 0.94 with AW + OSEM in the normal population. However, this ratio departed greatly from the reference ratio in pathologic patients, increasing to 2.3 in pathologic patients with reduced ^{99m}Tc cortical uptake instead of the expected 0.46. ANN + OSEM provides accurate relative activity quantitation in both normal and pathologic patients because it yields accurate absolute quantitation in these populations. For example, for the case just mentioned, the ratio of parietal cortex to cerebellum was 0.96 in normal patients and 0.45 in pathologic patients with ANN + OSEM.

Although high-energy photons are of low abundance (3.5%), they have an increased probability of penetrating through, or scattering in, the collimator and contributing to the spectral contamination. These photons should, therefore, not be neglected when simulating ^{123}I studies. For example,

when AW images were calculated without taking into account the high-energy contamination, the overestimations of the reference ^{99m}Tc activity distributions in the cerebellum and striata were 15% and 33%, respectively. These findings were in agreement with the experimental results of Dobbeleir et al. (*30*), who measured a high and uniform baseline contamination in air (scatter-to-photopeak ratio of 29%) over the 70–500 keV energy range at 20 cm from a LEHR collimator. In our study, the AW biases in the cerebellum and striata were reduced to 7% when a uniform background image was subtracted, as described in the discussion of cross-talk correction. However, even better accuracy (bias = 4%) was obtained with ANN by modeling the high-energy contamination photons in the training of the network.

CONCLUSION

We have proposed a new approach for absolute activity quantitation in dual ^{99m}Tc/^{123}I brain studies based on ANNs with error back-propagation as a learning tool, iterative OSEM, and three-dimensional recovery coefficients. This approach was evaluated in Monte Carlo simulated studies of normal and pathologic patients. Our results showed accurate quantitation of both radionuclides in both normal and pathologic populations. Moreover, ANN + OSEM clearly outperformed the simple windowing approach that led to important biases that varied not only between brain structures but also between normal and pathologic populations.

ACKNOWLEDGMENT

This study was supported in part by grants RO1-NS31902 and RO1-CA78936 from the National Institutes of Health (NIH). The contents of this article are solely the responsibility of the authors and do not represent the official views of NIH.

REFERENCES

1. Laruelle M, Wallace E, Seibyl JP, et al. Graphical, kinetic, and equilibrium analyses of in vivo [^{123}I] beta-CIT binding to dopamine transporters in healthy human subjects. *J Cereb Blood Flow Metab.* 1994;14:982–994.
2. Schwarz J, Antonini A, Tatsch K, Kirsch CM, Oertel WH, Leenders KL. Comparison of ^{123}I-IBZM SPECT and ^{11}C-raclopride PET findings in patients with parkinsonism. *Nucl Med Commun.* 1994;15:806–813.
3. Ichise M, Ballinger JR. SPECT imaging of dopamine receptors [editorial]. *J Nucl Med.* 1996;37:1591–1595.
4. Links JM. Simultaneous dual-radionuclide imaging: are the images trustworthy? *Eur J Nucl Med.* 1996;23:1289–1291.
5. Ivanovic M, Weber DA, Loncaric S, Franceschi D. Feasability of dual radionuclide brain imaging with I-123 and Tc-99m. *Med Phys.* 1994;21:667–674.
6. Devous MD, Lowe JL, Payne JK. Dual-isotope brain SPECT imaging with technetium and iodine-123: validation by phantom studies. *J Nucl Med.* 1992; 33:2030–2035.
7. Devous MD, Payne JK, Lowe JL. Dual-isotope brain SPECT imaging with technetium-99m and iodine-123: clinical validation using xenon-133 SPECT. *J Nucl Med.* 1992;33:1919–1924.
8. Ogawa K, Nishizaki N. Accurate scatter compensation using neural networks in radionuclide imaging. *IEEE Trans Nucl Sci.* 1993;40:1020–1025.
9. Maksud P, Fertil B, Rica C, El Fakhri G, Aurengo A. Artificial neural network as a tool to compensate for scatter and attenuation in radionuclide imaging. *J Nucl Med.* 1998;39:735–745.
10. El Fakhri G, Maksud P, Kijewski MF, et al. Scatter and cross-talk corrections in simultaneous Tc-99m/I-123 brain SPECT using constrained factor analysis and artificial neural networks. *IEEE Trans Nucl Sci.* 2000;47:1573–1580.
11. Zubal IG, Harrell CR, Simth EO, Rattner Z, Gindi G, Hoffer PB. Computerized three-dimensional segmented human anatomy. *Med Phys.* 1994;21:299–302.
12. Koyama M, Kawashima R, Ito H, et al. SPECT imaging of normal subjects with technetium-99m-HMPAO and technetium-99m-ECD. *J Nucl Med.* 1997;38:587–592.
13. Verhoeff NP, Kapucu O, Sokole-Busemann E, van Royen E, Janssen AG. Estimation of dopamine D2 receptor binding potential in the striatum with iodine-123-IBZM SPECT: technical and interobserver variability. *J Nucl Med.* 1993;34:2076–2084.
14. Madras BK, Gracz LM, Meltzer PC, et al. Altropane, a SPECT or PET imaging probe for dopamine neurons. II. Distribution to dopamine-rich regions of primate brain. *Synapse.* 1998;29:105–115.
15. Donnemiller E, Heilmann J, Wenning G, et al. Brain perfusion scintigraphy with ^{99m}Tc-HMPAO or ^{99m}Tc-ECD and ^{123}I-β-CIT single-photon emission tomography in dementia of the alzheimer-type and diffuse Lewy body disease. *Eur J Nucl Med.* 1997;24:320–325.
16. Harrison RL, Vannoy SD, Haynor DR, Gillispie SB, Kaplan MS, Lewellen TK. Preliminary experience with the photon history generator module of a public-domain simulation system for emission tomography. In: *Conference Record of the Nuclear Science Symposium.* 1993;2:1154–1158.
17. Haynor DR, Harrison RL, Lewellen TK. The use of importance sampling techniques to improve the efficiency of photon tracking in emission tomography simulations. *Med Phys.* 1991;18:990–1001.
18. de Vries DJ, Moore SC, Zimmerman RE, Mueller SP, Friedland B, Lanza RC. Development and validation of a Monte Carlo simulation of photon transport in an Anger camera. *IEEE Trans Med Imaging.* 1990;9:430–438.
19. Rumelhart D, Hinton G, Williams R. Learning internal representation by error propagation. In: Rumelhart DE, McClelland, JL, eds. *Parallel Distributed Processing: Explorations in the Microstructures of Cognition*. Cambridge, MA: MIT; 1986:318–362.
20. El Fakhri G, Maksud P, Habert MO, Todd-Pokropek A, Aurengo A. A new correction method for cross-talk using artificial neural networks: validation in simultaneous technetium and iodine cerebral imaging. In: *Conference Record of the Nuclear Science Symposium* [book on CD-ROM]. New York, NY: IEEE; 1999.
21. Masters T. Practical neural network recipes in C++. San Diego, CA: Academic Press; 1993:195–199.
22. Hudson HM, Larkin RS. Accelerated image reconstruction using ordered subsets of projection data. *IEEE Trans Med Imaging.* 1994;13:601–609.
23. Snyder DL, Miller MI. The use of sieves to stabilize images produced with the EM algorithm for emission tomography. *IEEE Trans Nucl Sci.* 1985;32:3864–3872.
24. Hoffman EJ, Huang SC, Phelps ME. Quantitation in positron emission computed tomography. 1. Effect of object size. *J Comput Assist Tomogr.* 1979;3:299–308.
25. Kojima A, Matsumoto M, Takahashi M, Hirota Y. Effect of spatial resolution on SPECT quantification values. *J Nucl Med.* 1989;30:508–514.
26. El Fakhri G, Buvat I, Benali H, Todd-Pokropek A, Di Paola R. Relative impact of scatter, attenuation, collimator response and finite resolution corrections in cardiac SPECT. *J Nucl Med.* 2000;41:1400–1408.
27. Da Silva A, Tang R, Wong K, Wu M, Dae M, Hasegawa B. Absolute in vivo quantitation of myocardial activity. In: *Conference Record of the Nuclear Science Symposium* [book on CD-ROM]. New York, NY: IEEE; 1999.
28. Siegel S, Castellan NJ. *Nonparametric Statistics for the Behavioral Sciences*. New York, NY: McGraw-Hill; 1988:144–151.
29. Gilland DR, Jaszczak RJ, Turkington TG, Greer KL, Coleman RE. Volume and activity quantitation with iodine-123 SPECT. *J Nucl Med.* 1994;35:1707–1713.
30. Dobbeleir AA, Hambÿe AS, Ranken PR. Influence of high-energy photons on the spectrum of iodine-123 with low- and medium-energy collimators: consequences for imaging with I-123 labelled compounds in clinical practice. *Eur J Nucl Med.* 1999;26:655–658.